Geophysical Research Letters

RESEARCH LETTER
10.1029/2022GL102285

Key Points:

- A novel process-oriented phase space reveals coherent patterns of terrestrial hydroclimate change
- Patterns emphasize the impact of soil moisture on temperature extremes and the redistribution of rainfall toward more intense events
- Patterns of $P - E$ changes reveal how land differs from the wet-get-wetter/dry-get-drier paradigm

Supporting Information:

Supporting Information may be found in the online version of this article.

Correspondence to:

S. Q. Duan,
sduan@princeton.edu

Citation:

Duan, S. Q., Findell, K. L., & Fueglistaler, S. A. (2023). Coherent mechanistic patterns of tropical land hydroclimate changes. *Geophysical Research Letters*, *50*, e2022GL102285. https://doi.org/10.1029/2022GL102285

Received 28 NOV 2022
Accepted 30 MAR 2023

© 2023. The Authors.
This is an open access article under the terms of the Creative Commons Attribution-NonCommercial-NoDerivs License, which permits use and distribution in any medium, provided the original work is properly cited, the use is non-commercial and no modifications or adaptations are made.

Coherent Mechanistic Patterns of Tropical Land Hydroclimate Changes

Suqin Q. Duan[1], Kirsten L. Findell[2], and Stephan A. Fueglistaler[1,3]

[1]Program in Atmospheric and Oceanic Sciences, Princeton University, Princeton, NJ, USA, [2]NOAA/Geophysical Fluid Dynamics Laboratory, Princeton, NJ, USA, [3]Department of Geosciences, Princeton University, Princeton, NJ, USA

Abstract Changes in tropical (30 S–30 N) land hydroclimate following CO_2-induced global warming are organized according to climatological aridity index (AI) and daily soil moisture (SM) percentiles. The transform from geographical space to this novel process-oriented phase space allows for interpretation of local, daily mechanistic relationships between key hydroclimatic variables in the context of time-mean and/or global-mean energetic constraints and the wet-get-wetter/dry-get-drier paradigm. Results from 16 CMIP models show coherent patterns of change in the AI/SM phase space that are aligned with the established soil-moisture/evapotranspiration regimes. We introduce an active-rain regime as a special case of the energy-limited regime. Rainfall shifts toward larger rain totals in this active-rain regime, with less rain on other days, resulting in an overall SM reduction. Consequently, the regimes where SM constrains evapotranspiration become more frequently occupied, and corresponding hydroclimatic changes align with the position of the critical SM value in the AI/SM phase space.

Plain Language Summary Predictions of terrestrial hydroclimate changes (temperature, precipitation, evaporation, etc.) in a warming world rely largely on model simulations with often diverging results when presented in map view. Here, we introduce a process-based phase space that organizes the spatial complexity by climatological aridity, and organizes the temporal complexity by daily soil moisture (SM). This allows for the analysis of model predictions in a comprehensive yet compact display which clearly reveals the connections between variables and mechanisms responsible for changes. Key results include the impact of SM limitation on elevated temperature extremes and the repartitioning of rainfall toward fewer, stronger events. This compact display is an efficient new tool for intercomparisons between models. The remarkably clean results suggest quantitative theoretical advances are possible despite the complexity of the system.

1. Introduction

Temperature and precipitation are dominant factors controlling the abundance and form of life on Earth. The intrinsic coupling between atmospheric temperature and the strength of the hydrological cycle is well understood (Betts & Ridgway, 1988; Jeevanjee & Fueglistaler, 2020; Jeevanjee & Romps, 2018; Manabe & Wetherald, 1967; P. A. O'Gorman et al., 2012; Pendergrass & Hartmann, 2014a). Under forcing from changes in greenhouse-gases such as carbon dioxide, the atmospheric radiative cooling increases, and correspondingly the hydrological cycle intensifies, and global average evaporation and precipitation increase (Allen & Ingram, 2002; Betts & Ridgway, 1988; Boer, 1993; Held & Soden, 2006). Model calculations and observations indicate that under global warming global atmospheric relative humidity changes little, and consequently specific humidity scales with the saturation vapor pressure and increases at the rate given by the Clausius-Clapeyron equation (Held & Soden, 2000, 2006; P. O'Gorman & Muller, 2010; Trenberth et al., 2005). Correspondingly, strong rainfall events scale like, or even exceed, the atmospheric specific humidity (Fildier et al., 2017; Muller et al., 2011; P. A. O'Gorman, 2015; P. A. O'Gorman & Schneider, 2009; Pendergrass & Hartmann, 2014b; Romps, 2011).

Numerical climate model simulations further provide a geographically more detailed prediction of local hydroclimatic changes with warming, whereby the simulations suggest generally a response known as "wet-get-wetter/dry-get-drier." This response pattern is expected for an atmosphere where the geographical pattern of atmospheric moisture convergence scales like the atmospheric water vapor (which scales approximately like the saturation vapor pressure, i.e., the Clausius-Clapeyron rate) and changes in atmospheric circulation are secondary. Since the atmospheric moisture convergence equals the difference between precipitation (P) and evaporation (E), that is, $P - E$, global warming will lead to an amplification of the

present-day geographical pattern of $P - E$ (Held & Soden, 2006). This result, however, requires in addition to a fixed atmospheric circulation, an unlimited moisture source at the surface. Over land, since evapotranspiration is constrained by soil moisture (SM), which in turn depends on the past evolution of $P - E$, the atmospheric convergence argument underlying the wet-get-wetter/dry-get-drier result may be less applicable (Byrne & O'Gorman, 2015; Chadwick et al., 2013; Greve et al., 2014; Greve & Seneviratne, 2015; Held & Soden, 2006).

Climate model simulations suggest over land a mean decrease of surface SM with warming (Berg et al., 2016, 2017; Berg & Sheffield, 2018; Cheng et al., 2017; Dai, 2013; IPCC, 2014). Along with this surface soil drying, an increase in the frequency of hotter, drier days is also widely demonstrated (Berg et al., 2014; Dirmeyer et al., 2021; Donat et al., 2017; Fischer et al., 2007; McKinnon et al., 2021; Seneviratne et al., 2013; Vogel et al., 2017). Conversely, wetter conditions seem to be indicated by studies reporting increased evapotranspiration (Greve et al., 2014; Jung et al., 2010) and increased occurrences of more extreme precipitation, flooding, and runoff (Donat et al., 2016; Hirabayashi et al., 2013; Kooperman et al., 2018; P. A. O'Gorman, 2015; Tabari, 2020). These seemingly divergent conclusions regarding drying or moistening of the land surface reflect the complexity of hydroclimatic changes over land, and make it difficult to formulate a concise and coherent terrestrial analog to the wet-get-wetter/dry-get-drier result for a fixed circulation over ocean.

In the following, we analyze climate model simulations in a novel process-based phase space that facilitates interpretation of changes in land hydroclimate in terms of theoretical arguments from an atmospheric convergence perspective *vis-a-vis* the land/vegetation-process perspective that emphasizes the non-linear relationship between SM and evapotranspiration.

2. Data and Method

2.1. Climate Models and Experiments

We analyze changes in land hydroclimate following forcing from increasing atmospheric carbon dioxide in simulations submitted to the Climate Model Intercomparison Project Phase 5 (Taylor et al., 2012) and Phase 6 (Eyring et al., 2016). The change is calculated as the difference between the last 30 years (20 years for MRI-CGCM3) of the abrupt-4 $\times$ CO_2 experiment minus the 30 years of the pre-industrial control simulation (following the "piControl" protocol) for CMIP5, and the 30 years over 1850–1880 of the historical simulation (following the "historical" protocol) for CMIP6. Results using simulations with gradual CO_2 increase instead of abrupt 4 $\times$ CO_2 are very similar (not shown).

Our analysis focuses on the tropics and the subtropics (i.e., 30°S–30°N) where surface conditions have a fairly tight connection to deep convective activity, and as such to the tropical climate (Emanuel et al., 1994; Romps, 2014; Zhang & Fueglistaler, 2020). The analysis is further narrowed to the warm season when land-atmosphere coupling is strongest and extreme events (heat extremes, rainfall or lack thereof) may have particularly pronounced impacts on society. The warm season is defined as the 150 days centered on 15 July for the Northern Hemisphere, and 150 days centered on 15 January for the Southern Hemisphere, giving a total of 4,500 days (30 years times 150 days) for each simulation. Results using data of the full calendar year are similar but have smaller amplitudes (see Figure S1 in Supporting Information S1).

Results are based on a total of 16 climate models that submitted the complete set of data for variables we require at daily (or sub-daily) resolution, with eight CMIP5 models (GFDL-ESM2M, CanESM2, ACCESS1-0, ACCESS1-3, FGOALS-g2, MRI-CGCM3, MIROC5, and NorESM1-M) and eight CMIP6 models (CanESM5, MIROC6, GFDL-CM4, MRI-ESM2-0, MPI-ESM1-2-HR, IPSL-CM6A-LR, CMCC-ESM2, INM-CM5-0). This list restricts the models to one model per modeling center (unless the schemes of particular relevance to simulations of the land hydroclimate are different, e.g., ACCESS1-0 and ACCESS1-3 use different land surface and cloud schemes), and also excludes simulations with inconsistent definition of variables (e.g., CNRM-CM5 reports SM in the top 1-cm layer instead of the top 10-cm layer). The land hydroclimate is characterized by the following variables: surface SM (moisture in the top 10 cm soil layer; SM), surface latent heat flux (LH, and as such also evapotranspiration ET), daily maximum surface air temperature ($\hat{T}$), precipitation (P), and surface air temperature (T). The calculation of the climatological aridity index (AI) further uses the downwelling and upwelling shortwave and longwave radiation fluxes at the surface in the reference simulations.

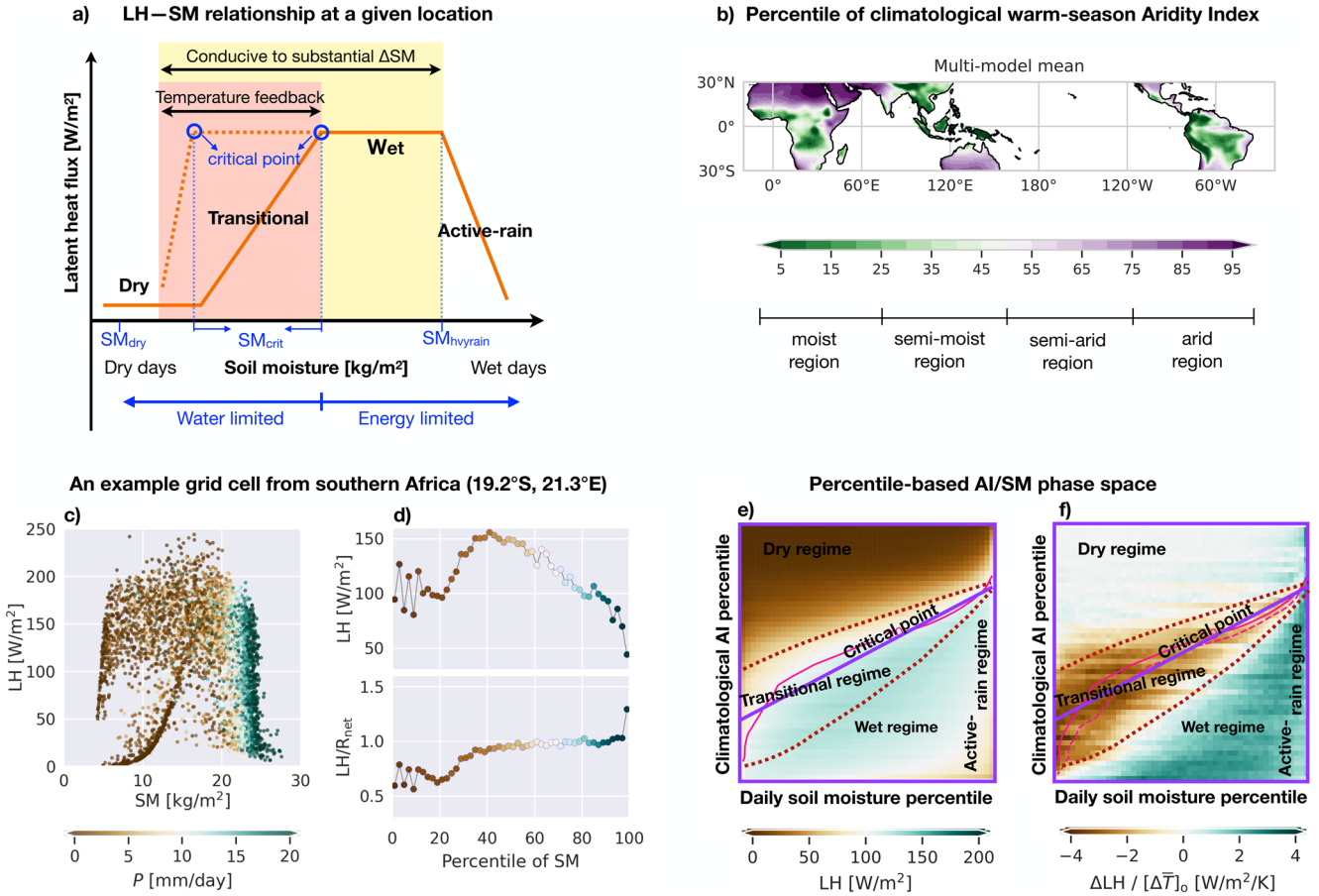

Figure 1. (a) Schematic of the regimes of surface latent heat flux (LH) as a function of surface soil moisture (SM; top 10 cm): The dry regime is near the lower SM limit; in the transitional regime SM and evapotranspiraton are tightly coupled; in the wet regime, past the critical point (SM_{crit}), SM is not the limiting factor for evapotranspiration; and in the active-rain regime evapotranspiration is limited by radiation and high boundary layer relative humidity. The transitional regime has two mechanistic pathways: the transpiration path (dashed orange line) where large changes in LH occur with small changes in SM, and the bare soil evaporation path (solid orange line) with typically smaller sensitivity of LH to SM. (b) The geographical pattern of the CMIP5 multi-model mean climatological warm-season aridity index (AI) percentiles (color coded) in the tropics, with qualitative labeling of quartiles (moist, semi-moist, semi-arid and arid). (c) The LH–SM relationship at an example grid cell from southern Africa in the base climate state (piControl) in GFDL-ESM2M: each dot represents 1 day (4,500 days in total), and the color corresponds to daily mean precipitation rate. (d) LH (upper panel) and evaporative fraction (LH/R_{net}, lower panel) sorted by and aggregated into local SM percentile bins at this example grid cell; markers are color-coded by the precipitation rate in the corresponding SM percentile bins. (e, f) Schematic of the SM regimes in the daily SM percentile/climatological AI percentile phase space. The background color corresponds to CMIP5 multi-model mean (e) LH in the base climate state and (f) changes in LH between the $4 \times CO_2$ and the piControl climate states, normalized by the mean tropical ocean warming $\left[\Delta\overline{T}\right]_o$.

2.2. The Soil Moisture-Evapotranspiration Relationship Over Land

The SM limitation on evapotranspiration (ET, or LH) substantially contributes to the complexity of climate change over land. The non-linear relationship between SM and ET largely determines how available energy is partitioned between latent, sensible, and ground heat fluxes. The schematic in Figure 1a (following Budyko et al., 1974; R. D. Koster et al., 2004; R. Koster et al., 2009; Seneviratne et al., 2010; Schwingshackl et al., 2017) shows four behavioral regimes connecting ET and SM: the dry regime, where ET is close to zero, the transitional regime, where ET increases monotonically with SM, the wet regime where ET is not determined by SM but rather by radiative energy availability, and an active-rain regime where ET is strongly limited due to high boundary layer relative humidity and energy limitations from cloudiness. Rainfall is not zero outside the active rain regime, but it is the dominant factor in this regime. Daily SM, LH, and precipitation data from an example grid cell in southern Africa from GFDL-ESM2M are shown in Figure 1c. The high precipitation rates and sharp drop-off of ET at high SM values indicate the need to introduce the active-rain regime. This regime is discussed further below, and is supported by plots of surface air relative humidity and surface net radiation in Figure S2 in Supporting Information S1.

The critical SM point, SM_{crit} (Figure 1a), separates moisture-limited days (in both the dry and transitional regimes) from energy-limited days (in both the wet and active-rain regimes). This critical point is dependent on soil and vegetative properties and is variable in space and time because dynamic roots can extend below the monitored SM zone (here 10 cm) and substantially increase access to moisture and alter the position of SM_{crit} in this functional relationship (illustrated as the dashed orange line in Figure 1a). It is in the transitional water-limited regime that SM conditions, vegetation types and plant physiological processes have the largest impact on surface climate (Seneviratne et al., 2010; Gentine et al., 2019, see also Figure S2 in Supporting Information S1 for the temperature condition in correspondence to Figure 1c). Correspondingly, biases and differences among models may lead to significant errors and uncertainty in predictions of ET and temperature. The frequently used evaporative fraction (Budyko et al., 1974; R. D. Koster et al., 2004; R. Koster et al., 2009; Seneviratne et al., 2010; Findell et al., 2011), defined as the ratio of the LH to the net radiative flux (R_{net}), does not separate the active-rain regime from the wet regime since it approaches unity in both energy-limited regimes and remains close to unity during active rainfall as both LH and R_{net} decrease. This can be seen in Figure 1d, where LH (upper panel) and the evaporative fraction (lower panel) are plotted against the SM percentiles at this location. Above the local 40th SM percentile, evaporative fraction stays close to 1, while LH decreases. That is, evaporative fraction cannot resolve the important hydroclimatic dynamics in this regime discussed in Sections 3 and 4.

2.3. The Aridity/Soil Moisture Phase Space

The daily model output is mapped from geographical space to a phase space (Figure 1e) defined by the climatological AI of a given location (y-axis) and the daily SM (x-axis). Both variables are transformed from their absolute value to their percentile rank in the distribution of the climatological AI in the tropics and subtropics, and in the distribution of daily SM at each grid cell over the period considered (see Section 2.1). For the climatological AI, we adopt the energy-based definition in (Milly & Dunne, 2016), which uses an estimate of potential evapotranspiration (PET) that is both simple and produces a better match of hydrological sensitivity to warming in climate models than other PET estimates:

$$\mathrm{AI} = \mathrm{PET}/P = 0.8 \cdot \mathrm{R}_{\mathrm{net}}^{\mathrm{sfc}}/(L_v \cdot P),$$

where P is precipitation, $\mathrm{R}_{\mathrm{net}}^{\mathrm{sfc}}$ is the net surface radiative flux, and L_v is the LH of vapourization. The constant 0.8 is set empirically to take into account the observational fact that not all available energy goes into ET even if surface water is not limited (Milly & Dunne, 2016; R. D. Koster & Mahanama, 2012). Figure 1b shows the geographic distribution of AI percentiles.

The transform into percentile space groups the regimes by specific physical conditions (e.g., dryness of the surface), and facilitates interpretation compared to the spatially-aggregated joint histograms or temporally/spatially averaged values of a variable (e.g., evapotranspiration, precipitation, or temperature). The daily SM percentile shows the temporal dynamic range of SM, and the separation by climatological AI ensures averaging over locations (grid cells) with similar distributions of daily SM. Thus, the SM percentile axis represents temporal variations in daily SM (from wet days to dry days) averaged over locations with equal AI percentile, and the AI percentile axis represents the geographical climatological separation of locations, ranging from very moist tropical rainfall regions (low AI percentile) to deserts (high AI percentile). Each area element in this 2-dimensional percentile phase space carries equal weight in terms of both the amount of days and the amount of the land area it represents; therefore, differences plotted in this phase space (e.g., LH changes shown in Figure 1f) quickly reveal the percent of time and space that experience certain changes (here in Figure 1f, i.e., decrease or increase of ET).

Changes in the magnitude of a variable X in the AI/SM phase space are calculated as the difference of the value in the $4 \times CO_2$ experiment minus the reference simulation (see Section 2.1), normalized by the mean warming over ocean to account for the different climate sensitivities among models. When mapping onto the AI axis, both the $4 \times CO_2$ and the reference simulations are sorted by the AI values in the reference simulation. Figures 1e and 1f show that the AI/SM phase space recovers the evapotranspiration regimes discussed above. As illustrated in Figure 1d for a single grid cell, the regimes capture the shape of LH as function of SM. In the SM/AI phase space (Figure 1e), the tropics as a whole have the LH at its minimum in the dry regime, it increases with SM (positive gradient) in the transitional regime, its change slows down in the wet regime, and then it decreases in the active rain regime. For the multi-model mean changes in LH following global warming (Figure 1f), the change is negligible in the climatologically dry regions (large AI), increases during days where a location is in the wet or active

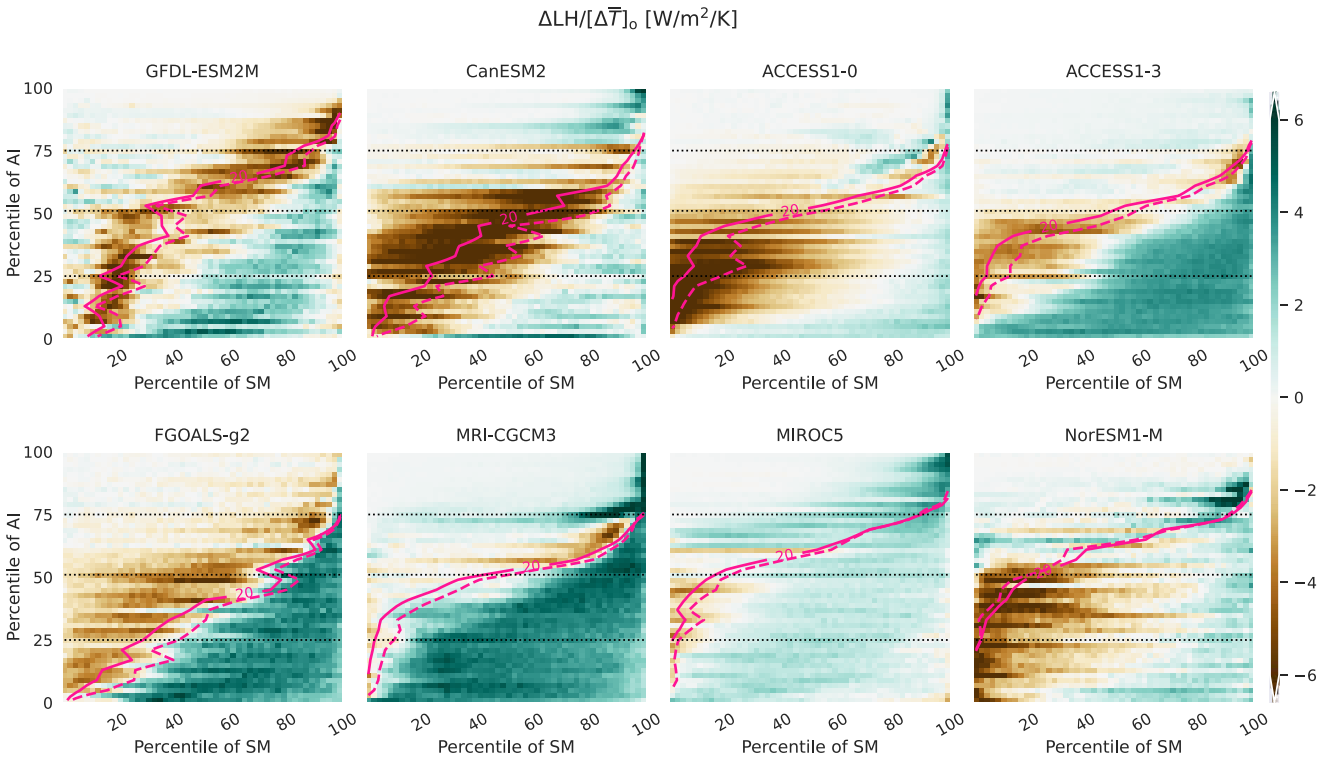

Figure 2. Changes of evapotranspiration (surface latent heat flux; W m^{-2}) in eight CMIP5 climate models in response to an abrupt quadrupling of CO_2 in the novel aridity index (AI)/soil moisture (SM) phase space. The *y*-axis is climatological AI percentiles, and the *x*-axis is local daily SM percentiles. Changes are normalized by the mean tropical ocean warming in each simulation. The pink lines show the surface SM isoline of 20 kg m^{-2} in the top 10 cm (an indicator of the critical SM value) in the base state (piControl, solid lines) and the perturbed climate state ($4 \times CO_2$, dashed lines).

rain regime, and decreases during days when a location is in the transitional regime around the critical point. By grouping locations and times with similar characteristics, the AI/SM phase space allows for a process-informed interpretation of the hydroclimatic changes over a large domain (here, tropics and subtropics) and time period.

3. Results

3.1. Evapotranspiration Changes in Individual Models

The map view of the projected warm-season mean changes in LH (normalized by mean ocean surface warming) in each of the eight CMIP5 models show large regional heterogeneity and prominent differences between models (Figure S3 in Supporting Information S1). For example, in key regions such as the Amazon and Australia, models lack consensus on even the projected sign of change. By contrast, Figure 2 shows the changes in ET (normalized by mean ocean surface warming) in each of the eight CMIP5 models (results for the CMIP6 models are similar) organized in the SM/AI phase space. All the models show ET reductions extending diagonally from the lower left corner to the upper right corner of the AI/SM phase space: The largest reductions in ET occur on days that are relatively dry in climatologically wet regions and on days that are relatively wet in climatologically dry regions. This band of reduced ET broadly aligns with the transitional regime. Above the transitional regime (at higher AI percentiles), the models show only small ET changes in the dry regime. To the right of the transitional regime (at higher SM percentiles), all models show increasing ET in the wet regime. Notably, ET in the wet regime increases at rates ($\lesssim$2%/K, not shown) similar to the rates of increase found over the ocean dictated by the increase in net atmospheric radiative cooling.

Despite the generally consistent patterns, differences between individual models in Figure 2 are particularly evident in the space-time extent and intensity of the ET change in the transitional regime. Growth of vegetation, changes in rooting depth and distribution, heterogeneity of sub-grid land tiles within a grid cell, and differences in soil texture and hydraulic properties among grid cells all contribute to variations in the value of the critical

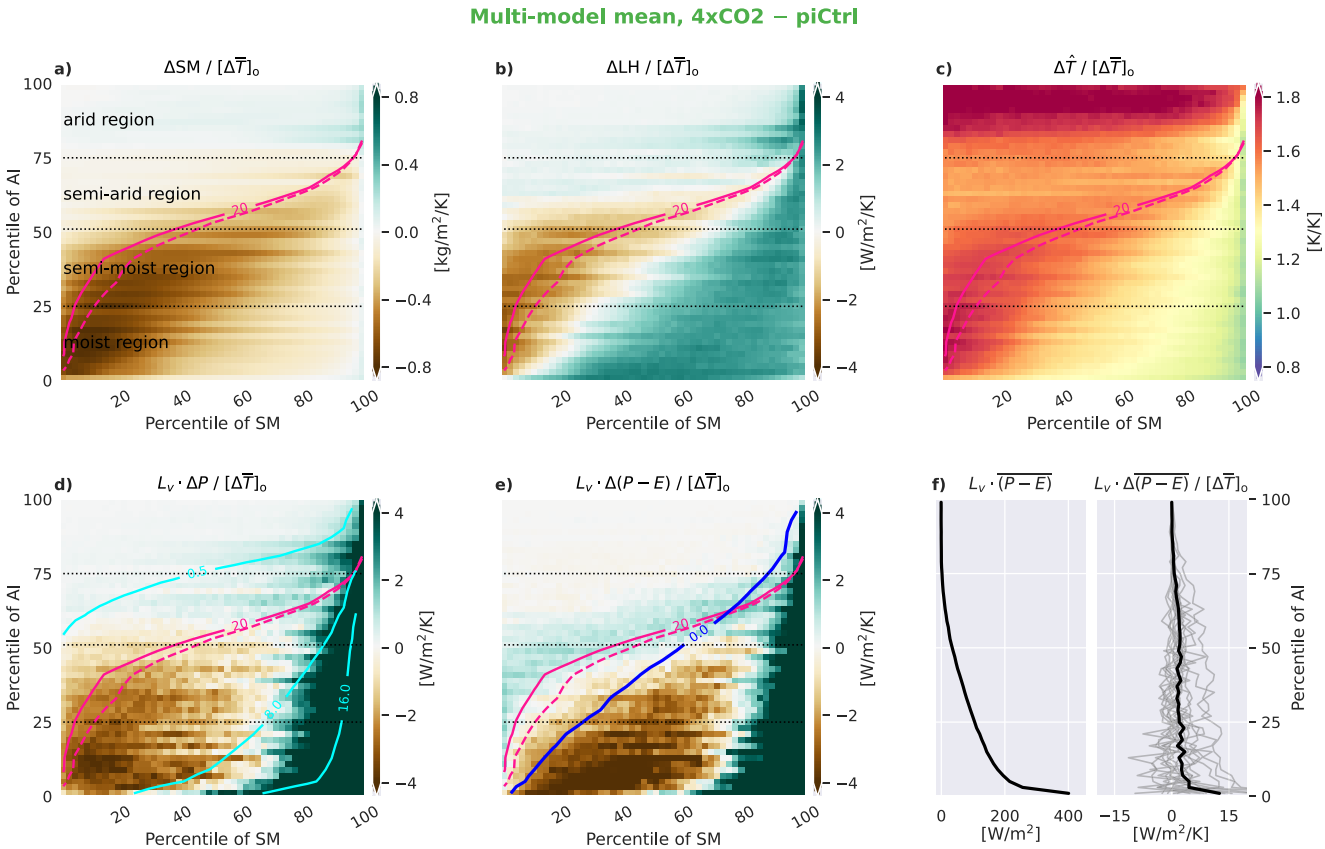

Figure 3. Multi-model mean (16 CMIP5 and CMIP6 models, see Section 2.1) changes in surface soil moisture (SM), latent heat flux (LH), daily-maximum temperature $(\hat{T})$, precipitation (P, times L_v to convert into the same unit as LH), and $P - E$ between the $4 \times CO_2$ and the base climate states, normalized by the simulation's mean tropical ocean warming $\left[\Delta\overline{T}\right]_o$. Pink lines show the SM value of 20 kg m^{-2} in the top 10 cm for the base (solid) and the $4 \times CO_2$ (dashed) climate states. The cyan curves in panel d show the base-climate precipitation rates of 0.5, 8 and 16 mm/day, and the blue curve in panel e shows the base-climate $P - E$ value of 0 W/m^2. Panel f shows the warm-season mean (panel e averaged over the x-axis) base-climate $P - E$ on the left and the change of it in the warm climate on the right. The thick black curve is the multi-model mean, and the gray lines are for individual models.

SM. However, the phase space employed here shows that a surface SM value of 20 kg m^{-2} in the top 10 cm of the ground (solid and dashed pink lines for the reference and $4 \times CO_2$ simulations respectively) aligns well with the drying pattern in most models, and we use this value as an approximation of SM_{crit} to analyze how regimes shift under global warming. In all but one model (NorESM1-M), the critical SM shifts toward higher SM percentiles (dashed pink line is to the right of solid pink line in 7 of 8 panels of Figure 2), indicating that locations are, over the course of the warm season, more frequently in the transitional regime in the warmer climate state.

To summarize, Figure 2 shows that the models exhibit a similar pattern of change arising from the LH–SM relationship, but they differ in the percentages of space and time that each regime occupies. Thus, while models may show disagreement for the predicted changes for specific regions (e.g., key regions such as the Congo or the Amazon, some models predict an increase and others a decrease in ET; Figure S3 in Supporting Information S1), they show coherent patterns in terms of changes for specific regimes.

3.2. Multi-Model Mean Hydroclimatic Change

Figure 3 summarizes the multi-model mean (average over all eight CMIP5 and eight CMIP6 models) prediction of changes in terrestrial hydroclimate between the $4 \times CO_2$ and the reference simulations. The separate panels show the change per unit ocean warming in SM, LH ($\propto$ ET), daily maximum temperature $(\hat{T})$, P, and $P - E$. As previously reported (Berg & Sheffield, 2018; Dai, 2013; IPCC, 2014), models predict a general decrease of surface SM (Figure 3a), but the decrease is uneven across time and space. The SM decrease peaks in both the

transitional and the wet regimes. In the transitional regime (around the critical SM value which is approximated by the pink line for SM at 20 kg m^{-2}; see Figure 2), evapotranspiration also decreases (Figure 3b); while in the wet regime, evapotranspiration is not SM limited and increases despite the decrease in SM. This indicates increasing atmospheric demand, stemming from higher R_{net} at the surface (not shown).

The daily maximum temperature ($\hat{T}$, Figure 3c) increases most in the dry regime (i.e., in the highest AI percentiles) as expected (e.g., Duan et al., 2020; Zhou, 2016), since the LH, and hence also changes therein, are negligible for the surface energy budget. The corresponding temperature increase is fairly uniform across all but the very highest SM percentiles where the models predict an increase in rainfall, SM and evapotranspiration. In the regions that are in the dry regime, the temperature distribution shifts to higher temperatures without changing shape (Duan et al., 2020).

In addition to the expected maximum in the dry regime, Figure 3c reveals a second maximum of daily maximum temperature increase that is aligned with the critical SM. In the transitional regime, a decrease in SM (see panel a) may shift a number of days from the wet regime with unconstrained evapotranspiration to the transitional or even dry regime with soil-moisture limited evaporation (panel b). The reduction in LH flux then leads to the second maximum of warming along the critical SM line.

In the generally moist regions (at low AI percentiles), the daily maximum temperatures increase most at low SM percentiles (i.e., when the region's SM is close to the critical SM), and least at high SM percentiles in the active rain regime. Days at low SM percentiles are warmer than days at high SM percentiles in the base climate, therefore the structure of warming we see here echoes previous findings for changes in the summertime temperature distribution shape: the warm tail of the temperature distribution shows amplified warming compared with the mean (Byrne, 2021; Donat et al., 2017; Duan et al., 2020; Vogel et al., 2017). These changes can be mapped back to geographic space to identify regions with enhanced vulnerability to heat extremes.

Figure 3d shows that precipitation changes little in the dry regime, decreases markedly in the transitional and wet regimes (the magnitude is about 0.1–0.2 mm/day per degree warming), and increases strongly in the active rain regime (high SM percentiles; the magnitude ranges from about 0.4 to 4 mm/day per degree warming). The very different changes in the wet and active rain regime shows the need to introduce the "active rain" regime, as the traditional "energy limited" regime (see Figure 1a) would average over rainfall changes with opposite signs. The large rainfall increases in the active rain regime reflect that extreme rainfall scales at rates similar to (or stronger than) the Clausius-Clapeyron scaling (Fildier et al., 2017; P. A. O'Gorman & Schneider, 2009; Pendergrass & Hartmann, 2014b; Pfahl et al., 2017). This rainfall increase is partly compensated by a decrease in rainfall totals at lower SM percentiles, consistent with a tendency toward stronger but fewer rain events (Lau et al., 2013; Pendergrass & Hartmann, 2014b).

Finally, Figure 3e shows the change in the difference between precipitation and evaporation ($P - E$). This term is at the heart of the wet-get-wetter/dry-get-drier paradigm describing changes over oceanic regions (Held & Soden, 2006) discussed above. Figure 3e shows that when examined in the AI/SM phase space, the pattern of changes in $P - E$ aligns with the SM regimes, indicating that the novel phase space employed here can help to interpret similarities and differences between changes over land and the wet-get-wetter/dry-get-drier paradigm, as discussed below.

4. Discussion

The transformation from geographical space to the AI/SM phase space of the key variables characterizing land climate properties facilitates the discussion of the changes in terms of the two canonical, complementary perspectives: On the one hand, the local perspective that emphasizes the importance of the SM constraint on evapotranspiration, and on the other hand the global perspective that emphasizes the global constraints on atmospheric moisture fluxes and their convergence.

Land as a whole is a region of net atmospheric moisture convergence and correspondingly $P - E \geq 0$ when integrated over the climatological annual cycle. Taken at face value, the wet-get-wetter perspective would predict on average an increase in $P - E$, which one may interpret as a tendency toward overall moister conditions. The AI/SM phase space allows us to look beyond the time-mean picture (e.g., the 5 months warm-season considered here) and explore the redistribution of $P - E$ on daily timescales, and how that redistribution depends on SM regime.

Figure 3e shows that there is very little change in $P - E$ in the dry regime, modest increases in the transitional regime, decreases in the wet regime, and sharp increases in the active rain regime. The change in rainfall (Figure 3d) drives the change in $P - E$ in the wet regime and active rain regimes: in both regimes evapotranspiration increases, but rainfall decreases in the wet regime and increases in the active-rain regime. The x-axis of the SM/AI phase space is daily SM, so the drying/wetting contrast in Figure 3e indicates that it is the wettest *days* that get wetter in a warmer world. The large temporal redistribution of $P - E$ over land suggests that the time-mean change in $P - E$ averaged over all land may be of secondary importance to understand the change of the land hydroclimate with global warming. In fact, Figure 3f, right panel, shows the time-mean change in $P - E$ (i.e., Figure 3e averaged over the x axis). The figure shows that upon warming, only a few models show a clear increase in the time-mean, while most models and the multi-model mean show small or uncertain changes in the time-mean. It is the redistribution over time (expanding the x-axis into daily SM percentiles) that leads to the prominent pattern of changes in rainfall (Figure 3d) and $P - E$ (Figure 3e).

The pattern of a decrease in $P - E$ in the wet regime and an increase in $P - E$ in the active rain regime bears resemblance to the wet-get-wetter/dry-get-drier result, but with important differences: Unlike in the wet-get-wetter/dry-get-drier picture, the sign change does not align with the $P - E = 0$ isoline of the base state (Figure 3e, blue line). Instead, the base state $P - E = 0$ isoline is in rough alignment with the critical SM isoline which separates the transitional and wet regimes. Furthermore, the increase of $P - E$ in the transitional regime (the green color around the pink lines in Figure 3e) is driven by a reduction in E that is larger in magnitude than the reduction in P, resulting in reduced moisture divergence (therefore this positive change in $P - E$ should be interpreted as drying instead of moistening). The difference $P - E$ is, the difference between a slowly varying term (evapotranspiration; see the fairly homogeneous change in LH in the wet and active rain regimes in panel b) and a highly intermittent term (rainfall). Over ocean, the redistribution of precipitation has no impact on evaporation, but over land, the associated SM decrease (Figure 3a) shifts the percentile position of the critical SM value which indicates an increase in the fraction of time spent in the transitional and dry regimes where SM constrains evapotranspiration.

5. Summary and Outlook

Accurate predictions of future changes in hydroclimate over land, in particular the magnitude and frequency of extreme heat, extreme rainfall, and droughts are of paramount importance for society. Process-level understanding of land-atmosphere interactions has greatly improved, but there remain gaps in our understanding in particular with respect to: (a) the connection between changes in different types of extremes; and (b) the connection between changes in local land-atmosphere interactions with the global-scale thermodynamic and radiative constraints on the response of the hydrological cycle to climate forcings.

The process-oriented AI/SM phase space presented here preserves the mechanistic local, daily-mean time scale understanding as summarized in Figure 1a while substantially reducing the dimensionality of the global, time-varying problem in order to provide an integrated, big-picture perspective. Using this transformation from geographical/time space to the SM/AI phase space yields remarkably clear results (Figure 3), building physical intuition for the changes, and the coupling of changes between different variables. Specifically, model predictions (Figure 3) show for the tropical and subtropical warm season a robust and coherent pattern of change aligned with the widely used SM/evapotranspiration regimes, with individual model behavior and biases illuminated by the relative differences in the frequency of occurrence of each regime, shown here for changes in LH (Figure 2). The alignment of the change patterns with the widely used regimes (the moisture-limited dry and transitional regimes, and the energy-limited regime) demonstrates the importance of the critical SM separating energy- and moisture-limited conditions. Our analysis reveals the need to introduce the active-rain regime to further differentiate the conventional energy-limited regime when considering multiple aspects of hydroclimate changes. Contrasting behavior of changes in $P - E$ in these two regimes reflects the fact that rainfall is a highly intermittent process, balanced by the slowly-varying evapotranspiration. The reduction in rainfall at intermediate SM percentiles indicates a tendency to repartition the total rainfall toward fewer but stronger rainfall days. The AI/SM phase space clearly reveals how this effect has a pronounced impact for the land hydroclimate in that it pushes land for a larger fraction of time into the SM limited regime. As evident in Figure 3c, this regime shift also contributes to the larger warming over land relative to that over the oceans. Land hydroclimatic changes under global warming thus may not be understood from the present distribution of hydroclimate regimes alone, as changes in the occurrence frequency of the regimes can be similarly important.

The emergence of mechanistic, coherent patterns of land hydroclimate change in the AI/SM percentile phase space suggests that this phase space may prove useful for several applications. As the example of the different evapotranspiration changes (Figure 2) shows, the AI/SM phase space allows a compact, efficient identification of similarities and differences between models and possibly also between models and observations, and by virtue of retaining the daily timescale, allows a mechanistic interpretation thereof. Moreover, while the importance of the SM constraint on evapotranspiration is widely acknowledged, expansion of large-scale theories of changes in the hydrological cycle to properly account for this constraint remains incomplete. The emergence of clear patterns that can be sensibly interpreted mechanistically may provide new motivation and inspiration for a theory that bridges local and global constraints.

Data Availability Statement

CMIP5 and CMIP6 model outputs used in this study were downloaded from the CMIP data portal (https://esgf-node.llnl.gov/search/cmip5/ and https://esgf-node.llnl.gov/search/cmip6/), and the CEDA data archive (http://data.ceda.ac.uk/badc/cmip5/data/cmip5/output1/ and https://data.ceda.ac.uk/badc/cmip6/data/CMIP6/CMIP/). Data in these archives are openly available and can be downloaded by selecting names of models, experiments, and variables. The list of models, experiments, and variables used in this study are described in Section 2.1.

Acknowledgments
The authors acknowledge support from National Science Foundation Award NSF PIRE-1743753. We thank the climate modeling groups for producing and making available their model output, the Earth System Grid Federation (ESGF), and the Centre for Environmental Data Analysis (CEDA) for archiving the data and providing access, and the multiple funding agencies who support CMIP activities, ESGF, and CEDA. We thank Dr. Nadir Jeevanjee, Dr. Zhihong Tan, Dr. Khaled Ghannam for helpful conversations and internal reviews. We thank two anonymous reviewers for insightful and constructive reviews, and we thank the editor for handling the manuscript.

References

Allen, M. R., & Ingram, W. J. (2002). Constraints on future changes in climate and the hydrologic cycle. *Nature*, *419*(6903), 228–232. https://doi.org/10.1038/nature01092

Berg, A., Findell, K., Lintner, B., Giannini, A., Seneviratne, S. I., Van den Hurk, B., et al. (2016). Land–atmosphere feedbacks amplify aridity increase over land under global warming. *Nature Climate Change*, *6*(9), 869–874. https://doi.org/10.1038/nclimate3029

Berg, A., Lintner, B. R., Findell, K. L., Malyshev, S., Loikith, P. C., & Gentine, P. (2014). Impact of soil moisture–atmosphere interactions on surface temperature distribution. *Journal of Climate*, *27*(21), 7976–7993. https://doi.org/10.1175/jcli-d-13-00591.1

Berg, A., & Sheffield, J. (2018). Climate change and drought: The soil moisture perspective. *Current Climate Change Reports*, *4*(2), 180–191. https://doi.org/10.1007/s40641-018-0095-0

Berg, A., Sheffield, J., & Milly, P. C. (2017). Divergent surface and total soil moisture projections under global warming. *Geophysical Research Letters*, *44*(1), 236–244. https://doi.org/10.1002/2016gl071921

Betts, A. K., & Ridgway, W. (1988). Coupling of the radiative, convective, and surface fluxes over the equatorial Pacific. *Journal of the Atmospheric Sciences*, *45*(3), 522–536. https://doi.org/10.1175/1520-0469(1988)045<0522:cotrca>2.0.co;2

Boer, G. (1993). Climate change and the regulation of the surface moisture and energy budgets. *Climate Dynamics*, *8*(5), 225–239. https://doi.org/10.1007/bf00198617

Budyko, M. I., Miller, D. H., & Miller, D. H. (1974). *Climate and life* (Vol. 508). Academic press.

Byrne, M. P. (2021). Amplified warming of extreme temperatures over tropical land. *Nature Geoscience*, *14*(11), 837–841. https://doi.org/10.1038/s41561-021-00828-8

Byrne, M. P., & O'Gorman, P. A. (2015). The response of precipitation minus evapotranspiration to climate warming: Why the "wet-get-wetter, dry-get-drier" scaling does not hold over land. *Journal of Climate*, *28*(20), 8078–8092. https://doi.org/10.1175/jcli-d-15-0369.1

Chadwick, R., Boutle, I., & Martin, G. (2013). Spatial patterns of precipitation change in CMIP5: Why the rich do not get richer in the tropics. *Journal of Climate*, *26*(11), 3803–3822. https://doi.org/10.1175/jcli-d-12-00543.1

Cheng, S., Huang, J., Ji, F., & Lin, L. (2017). Uncertainties of soil moisture in historical simulations and future projections. *Journal of Geophysical Research: Atmospheres*, *122*(4), 2239–2253. https://doi.org/10.1002/2016jd025871

Dai, A. (2013). Increasing drought under global warming in observations and models. *Nature Climate Change*, *3*(1), 52–58. https://doi.org/10.1038/nclimate1633

Dirmeyer, P. A., Balsamo, G., Blyth, E. M., Morrison, R., & Cooper, H. M. (2021). Land-atmosphere interactions exacerbated the drought and heatwave over northern Europe during summer 2018. *AGU Advances*, *2*(2), e2020AV000283. https://doi.org/10.1029/2020av000283

Donat, M. G., Lowry, A. L., Alexander, L. V., O'Gorman, P. A., & Maher, N. (2016). More extreme precipitation in the world's dry and wet regions. *Nature Climate Change*, *6*(5), 508–513. https://doi.org/10.1038/nclimate2941

Donat, M. G., Pitman, A. J., & Seneviratne, S. I. (2017). Regional warming of hot extremes accelerated by surface energy fluxes. *Geophysical Research Letters*, *44*(13), 7011–7019. https://doi.org/10.1002/2017gl073733

Duan, S. Q., Findell, K. L., & Wright, J. S. (2020). Three regimes of temperature distribution change over dry land, moist land and oceanic surfaces. *Geophysical Research Letters*, *47*(24), e2020GL090997. https://doi.org/10.1029/2020GL090997

Emanuel, K. A., David Neelin, J., & Bretherton, C. S. (1994). On large-scale circulations in convecting atmospheres. *Quarterly Journal of the Royal Meteorological Society*, *120*(519), 1111–1143. https://doi.org/10.1002/qj.49712051902

Eyring, V., Bony, S., Meehl, G. A., Senior, C. A., Stevens, B., Stouffer, R. J., & Taylor, K. E. (2016). Overview of the Coupled Model Intercomparison Project Phase 6 (CMIP6) experimental design and organization. *Geoscientific Model Development*, *9*(5), 1937–1958. https://doi.org/10.5194/gmd-9-1937-2016

Fildier, B., Parishani, H., & Collins, W. (2017). Simultaneous characterization of mesoscale and convective-scale tropical rainfall extremes and their dynamical and thermodynamic modes of change. *Journal of Advances in Modeling Earth Systems*, *9*(5), 2103–2119. https://doi.org/10.1002/2017ms001033

Findell, K. L., Gentine, P., Lintner, B. R., & Kerr, C. (2011). Probability of afternoon precipitation in eastern United States and Mexico enhanced by high evaporation. *Nature Geoscience*, *4*(7), 434–439. https://doi.org/10.1038/ngeo1174

Fischer, E. M., Seneviratne, S. I., Lüthi, D., & Schär, C. (2007). Contribution of land-atmosphere coupling to recent European summer heat waves. *Geophysical Research Letters*, *34*(6), L06707. https://doi.org/10.1029/2006gl029068

Gentine, P., Massmann, A., Lintner, B. R., Hamed Alemohammad, S., Fu, R., Green, J. K., et al. (2019). Land–atmosphere interactions in the tropics–a review. *Hydrology and Earth System Sciences*, *23*(10), 4171–4197. https://doi.org/10.5194/hess-23-4171-2019

Greve, P., Orlowsky, B., Mueller, B., Sheffield, J., Reichstein, M., & Seneviratne, S. I. (2014). Global assessment of trends in wetting and drying over land. *Nature Geoscience*, *7*(10), 716–721. https://doi.org/10.1038/ngeo2247

Greve, P., & Seneviratne, S. I. (2015). Assessment of future changes in water availability and aridity. *Geophysical Research Letters*, *42*(13), 5493–5499. https://doi.org/10.1002/2015gl064127

Held, I. M., & Soden, B. J. (2000). Water vapor feedback and global warming. *Annual Review of Energy and the Environment*, *25*(1), 441–475. https://doi.org/10.1146/annurev.energy.25.1.441

Held, I. M., & Soden, B. J. (2006). Robust responses of the hydrological cycle to global warming. *Journal of Climate*, *19*(21), 5686–5699. https://doi.org/10.1175/jcli3990.1

Hirabayashi, Y., Mahendran, R., Koirala, S., Konoshima, L., Yamazaki, D., Watanabe, S., et al. (2013). Global flood risk under climate change. *Nature Climate Change*, *3*(9), 816–821. https://doi.org/10.1038/nclimate1911

IPCC. (2014). *Climate change 2013—The physical science basis: Working group I contribution to the fifth assessment report of the intergovernmental panel on climate change*. Cambridge University Press. https://doi.org/10.1017/CBO9781107415324

Jeevanjee, N., & Fueglistaler, S. (2020). Simple spectral models for atmospheric radiative cooling. *Journal of the Atmospheric Sciences*, *77*(2), 479–497. https://doi.org/10.1175/jas-d-18-0347.1

Jeevanjee, N., & Romps, D. M. (2018). Mean precipitation change from a deepening troposphere. *Proceedings of the National Academy of Sciences*, *115*(45), 11465–11470. https://doi.org/10.1073/pnas.1720683115

Jung, M., Reichstein, M., Ciais, P., Seneviratne, S. I., Sheffield, J., Goulden, M. L., et al. (2010). Recent decline in the global land evapotranspiration trend due to limited moisture supply. *Nature*, *467*(7318), 951–954. https://doi.org/10.1038/nature09396

Kooperman, G. J., Fowler, M. D., Hoffman, F. M., Koven, C. D., Lindsay, K., Pritchard, M. S., et al. (2018). Plant physiological responses to rising CO_2 modify simulated daily runoff intensity with implications for global-scale flood risk assessment. *Geophysical Research Letters*, *45*(22), 12–457. https://doi.org/10.1029/2018gl079901

Koster, R., Schubert, S., & Suarez, M. (2009). Analyzing the concurrence of meteorological droughts and warm periods, with implications for the determination of evaporative regime. *Journal of Climate*, *22*(12), 3331–3341. https://doi.org/10.1175/2008jcli2718.1

Koster, R. D., Dirmeyer, P. A., Guo, Z., Bonan, G., Chan, E., Cox, P., et al. (2004). Regions of strong coupling between soil moisture and precipitation. *Science*, *305*(5687), 1138–1140. https://doi.org/10.1126/science.1100217

Koster, R. D., & Mahanama, S. P. (2012). Land surface controls on hydroclimatic means and variability. *Journal of Hydrometeorology*, *13*(5), 1604–1620. https://doi.org/10.1175/jhm-d-12-050.1

Lau, W. K.-M., Wu, H.-T., & Kim, K.-M. (2013). A canonical response of precipitation characteristics to global warming from CMIP5 models. *Geophysical Research Letters*, *40*(12), 3163–3169. https://doi.org/10.1002/grl.50420

Manabe, S., & Wetherald, R. T. (1967). Thermal equilibrium of the atmosphere with a given distribution of relative humidity. *Journal of the Atmospheric Sciences*, *24*(3), 241–259. https://doi.org/10.1175/1520-0469(1967)024<0241:teotaw>2.0.co;2

McKinnon, K. A., Poppick, A., & Simpson, I. R. (2021). Hot extremes have become drier in the United States Southwest. *Nature Climate Change*, *11*(7), 598–604. https://doi.org/10.1038/s41558-021-01076-9

Milly, P. C., & Dunne, K. A. (2016). Potential evapotranspiration and continental drying. *Nature Climate Change*, *6*(10), 946–949. https://doi.org/10.1038/nclimate3046

Muller, C. J., O'Gorman, P. A., & Back, L. E. (2011). Intensification of precipitation extremes with warming in a cloud-resolving model. *Journal of Climate*, *24*(11), 2784–2800. https://doi.org/10.1175/2011jcli3876.1

O'Gorman, P., & Muller, C. J. (2010). How closely do changes in surface and column water vapor follow Clausius–Clapeyron scaling in climate change simulations? *Environmental Research Letters*, *5*(2), 025207. https://doi.org/10.1088/1748-9326/5/2/025207

O′Gorman, P. A. (2015). Precipitation extremes under climate change. *Current Climate Change Reports*, *1*(2), 49–59. https://doi.org/10.1007/s40641-015-0009-3

O'Gorman, P. A., Allan, R. P., Byrne, M. P., & Previdi, M. (2012). Energetic constraints on precipitation under climate change. *Surveys in Geophysics*, *33*(3), 585–608. https://doi.org/10.1007/s10712-011-9159-6

O'Gorman, P. A., & Schneider, T. (2009). The physical basis for increases in precipitation extremes in simulations of 21st-century climate change. *Proceedings of the National Academy of Sciences*, *106*(35), 14773–14777. https://doi.org/10.1073/pnas.0907610106

Pendergrass, A. G., & Hartmann, D. L. (2014a). The atmospheric energy constraint on global-mean precipitation change. *Journal of Climate*, *27*(2), 757–768. https://doi.org/10.1175/jcli-d-13-00163.1

Pendergrass, A. G., & Hartmann, D. L. (2014b). Changes in the distribution of rain frequency and intensity in response to global warming. *Journal of Climate*, *27*(22), 8372–8383. https://doi.org/10.1175/jcli-d-14-00183.1

Pfahl, S., O′Gorman, P. A., & Fischer, E. M. (2017). Understanding the regional pattern of projected future changes in extreme precipitation. *Nature Climate Change*, *7*(6), 423–427. https://doi.org/10.1038/nclimate3287

Romps, D. M. (2011). Response of tropical precipitation to global warming. *Journal of the Atmospheric Sciences*, *68*(1), 123–138. https://doi.org/10.1175/2010jas3542.1

Romps, D. M. (2014). An analytical model for tropical relative humidity. *Journal of Climate*, *27*(19), 7432–7449. https://doi.org/10.1175/jcli-d-14-00255.1

Schwingshackl, C., Hirschi, M., & Seneviratne, S. I. (2017). Quantifying spatiotemporal variations of soil moisture control on surface energy balance and near-surface air temperature. *Journal of Climate*, *30*(18), 7105–7124. https://doi.org/10.1175/jcli-d-16-0727.1

Seneviratne, S. I., Corti, T., Davin, E. L., Hirschi, M., Jaeger, E. B., Lehner, I., et al. (2010). Investigating soil moisture–climate interactions in a changing climate: A review. *Earth-Science Reviews*, *99*(3–4), 125–161. https://doi.org/10.1016/j.earscirev.2010.02.004

Seneviratne, S. I., Wilhelm, M., Stanelle, T., Hurk, B., Hagemann, S., Berg, A., et al. (2013). Impact of soil moisture-climate feedbacks on CMIP5 projections: First results from the GLACE-CMIP5 experiment. *Geophysical Research Letters*, *40*(19), 5212–5217. https://doi.org/10.1002/grl.50956

Tabari, H. (2020). Climate change impact on flood and extreme precipitation increases with water availability. *Scientific Reports*, *10*(1), 1–10. https://doi.org/10.1038/s41598-020-70816-2

Taylor, K. E., Stouffer, R. J., & Meehl, G. A. (2012). An overview of CMIP5 and the experiment design. *Bulletin of the American Meteorological Society*, *93*(4), 485–498. https://doi.org/10.1175/BAMS-D-11-00094.1

Trenberth, K. E., Fasullo, J., & Smith, L. (2005). Trends and variability in column-integrated atmospheric water vapor. *Climate Dynamics*, *24*(7), 741–758. https://doi.org/10.1007/s00382-005-0017-4

Vogel, M. M., Orth, R., Cheruy, F., Hagemann, S., Lorenz, R., Hurk, B., & Seneviratne, S. I. (2017). Regional amplification of projected changes in extreme temperatures strongly controlled by soil moisture-temperature feedbacks. *Geophysical Research Letters*, *44*(3), 1511–1519. https://doi.org/10.1002/2016gl071235

Zhang, Y., & Fueglistaler, S. (2020). How tropical convection couples high moist static energy over land and ocean. *Geophysical Research Letters*, *47*(2), e2019GL086387. https://doi.org/10.1029/2019gl086387

Zhou, L. (2016). Desert amplification in a warming climate. *Scientific Reports*, *6*(1), 31065. https://doi.org/10.1038/srep31065